How Moist and Dry Intrusions Control the Local Hydrologic Cycle in Present and Future Climates

SAMUEL SMITH,[a] PAUL W. STATEN,[a] AND JIAN LU[b]

[a] *Indiana University Bloomington, Bloomington, Indiana*
[b] *Pacific Northwest National Laboratory, Richland, Washington*

(Manuscript received 6 October 2020, in final form 14 January 2021)

ABSTRACT: Models disagree on how much the hydrologic cycle could intensify under climate change. These changes are expected to scale with the Clausius–Clapeyron relation but may locally diverge due in part to the uncertain response of the general circulation, causing the hydrologic cycle to inherit this uncertainty. To identify how the circulation contributes, we link circulation changes to changes in the higher moments of the hydrologic cycle using the novel dynamical framework of the local hydrologic cycle, the portion of the hydrologic cycle driven by moist or dry intrusions. We expand this dynamical framework, developing a closed budget that diagnoses thermodynamic, advective, and overturning contributions to future hydrologic cycle changes. In analyzing these changes for the Community Earth System Model Large Ensemble, we show that overturning is the main dynamic contributor to the tropical and subtropical annual response, consistent with a weakening of this circulation. In the extratropics, we show that advective contributions, likely from storm track changes, dominate the response. We achieve a cleaner separation between dynamic and thermodynamic contributions through a semiempirical scaling, which reveals the robustness of the Clausius–Clapeyron scaling for the local hydrologic cycle. This scaling also demonstrates the slowing of the local hydrologic cycle and how changing subtropical dynamics asymmetrically impact wave breaking and suppress meridional moisture transport. We conclude that dynamic changes in the subtropics are predominantly responsible for the annual, dynamic response in the extratropics and thus a significant contributor to uncertainty in future projections.

KEYWORDS: Atmospheric circulation; Hydrologic cycle; Nonlinear dynamics; Climate change; Moisture/moisture budget; General circulation models

1. Introduction

Climate change will intensify the hydrologic cycle, both in the mean and the extremes (Trenberth 1999; Allen and Ingram 2002; Held and Soden 2006; O'Gorman and Schneider 2009; O'Gorman 2015; Chen et al. 2019). While this intensification will not be spatially uniform (Neelin et al. 2013; Polade et al. 2017; Lu et al. 2018; Song et al. 2018; Feng et al. 2019), confidence in this intensification stems from global energy constraints (Trenberth 1999; Held and Soden 2006) and basic thermodynamic principles (Lorenz and DeWeaver 2007; Stephens and Hu 2010). Regionally, the magnitude of hydrologic cycle changes is less certain, despite clear thermodynamic signals (O'Gorman 2015; Pfahl et al. 2017). This uncertainty is largely due to uncertainty in atmospheric circulation changes, often termed the "dynamic" response (Lu et al. 2014; O'Gorman 2015; Pfahl et al. 2017; Tandon et al. 2018; Weller et al. 2019), although other drivers of regional climate such as land–sea contrast may contribute (Byrne and O'Gorman 2015). Work to reduce uncertainty in regional changes has concentrated on isolating the dynamic or circulation-driven component of change across the probability distribution of the hydrologic cycle (O'Gorman and Schneider 2009; Seager et al. 2010; Bony et al. 2013; Pendergrass and Gerber 2016; Pfahl et al. 2017; Tandon et al. 2018; Weller et al. 2019; Chen et al. 2019).

Despite this recent effort, delineating between dynamically and thermodynamically driven changes in future projections of the hydrologic cycle remains a challenge, complicated by the nonlinearity of advection in the advection–diffusion–condensation problem, which controls the hydrologic cycle (Neelin et al. 2010; Lu et al. 2017). Consequently, statistical methods for decomposition that rely on the empirical correlation between precipitation amount and vertical velocity may be invalid in some regions, particularly the subtropics (Pfahl et al. 2017). Physically based methods that scale precipitation with the moist adiabatic lapse rate require assumptions of large-scale saturated ascent (Pfahl et al. 2017), and they cannot discriminate between the varied processes responsible for that ascent beyond the relative impacts of stability and the length scale of convergence (Tandon et al. 2018). Decompositions of the Eulerian column water vapor budget can result in various nonlinear or higher-order terms (Seager and Henderson 2013; Byrne and O'Gorman 2015; Lu et al. 2017), which are not always negligible and can be challenging to compute or interpret (Seager and Henderson 2013).

The heterogeneous nature of the dynamic component of hydrologic cycle change compounds these diagnostic challenges. This dynamic component aggregates many changes in the atmospheric circulation: at the largest scales, jet streams shift (Chang et al. 2012; Shaw 2019; Shaw et al. 2016) and

Supplemental information related to this paper is available at the Journals Online website: https://doi.org/10.1175/JCLI-D-20-0780.s1.

Corresponding author: Samuel Smith, samjsmit@iu.edu

DOI: 10.1175/JCLI-D-20-0780.1

Hadley circulations widen (Kang and Lu 2012; Lu et al. 2007; Staten et al. 2019); at local levels, circulations respond to increased land–sea contrast (Byrne and O'Gorman 2013; Joshi et al. 2008), dwindling sea ice (Kim et al. 2014; Romanowsky et al. 2019), and modified sea surface temperatures (Huang et al. 2017). Thus, narrowing the spread in future projections of regional hydrologic cycle changes requires process-level understanding (Liu et al. 2020; Polade et al. 2014).

However, understanding these dynamic changes in isolation neglects their interdependence (Pendergrass and Gerber 2016; Thackeray et al. 2018). Despite this, precipitation-producing ("wet") processes and precipitation-inhibiting ("dry") processes are often studied separately—a natural dichotomy given the highly skewed distribution of precipitation and the enormous range of climatological precipitation characteristics. While such wet and dry speciation has yielded substantial insight (Liu et al. 2020; al Fahad et al. 2020), it may obscure the relative contributions of wet and dry processes to the net response. For example, understanding future changes in rain rates requires understanding changes in both ascent and descent (Pendergrass and Gerber 2016). This interdependence motivates an approach that focuses on the driving circulations common to all wet and dry processes. To address this goal, we develop a hybrid Eulerian–Lagrangian framework to analyze the higher moments of the wet and dry ends of the hydrologic cycle in present and future climates, benefitting from both a closed budget equation and a diffusive scaling relationship.

Central to our effort is the local hydrologic cycle (LHC), introduced by Lu et al. (2017; hereafter L17). Intuitively, the LHC represents the net precipitation or evaporation driven by "zonally anomalous" moisture or dryness, which we refer to as moist or dry intrusions. However, the measure of zonal asymmetry used here is not the Eulerian zonal mean [as in, e.g., Wills et al. (2016)]. Rather, we measure zonal asymmetry with respect to a Lagrangian background state, which is more strongly constrained to Clausius–Clapeyron (CC) scaling than its Eulerian counterpart, as we will demonstrate. This approach enables an alternative perspective on the role of moisture transport process in dynamically and thermodynamically modifying the hydrologic cycle. We define the LHC more formally in section 2.

In introducing the LHC framework, L17 primarily focus on its zonal-mean formulation and its application to atmospheric rivers (ARs) and precipitation extremes. Lu et al. (2018; hereafter L18) confirm this robust connection between the LHC and more traditional metrics of precipitation extremes (see their Fig. 3) while also introducing the zonally varying LHC, which they use to examine changes in ARs in the western United States. Xue et al. (2018) similarly utilize the LHC framework to study the Asian summer monsoon. A prominent result of these previous works on the LHC is that the LHC slows in response to climate change in a manner analogous to that seen for the mean hydrologic cycle (i.e., Held and Soden 2006).

The structure of this work is outlined as follows. In section 2, we review the LHC framework and its assumptions, extend the moist framework of L17 and L18 to encompass the dry component of the LHC, and develop its closed budget equation analogous to the Eulerian moisture budget (e.g., Seager et al. 2010). In section 3, we describe the Community Earth System Model (CESM) Large Ensemble (LENS) dataset utilized here, along with challenges in the numerical implementation of the LHC framework. In section 4, we present our results, beginning by examining advective and overturning contributions from the LHC budget in section 4a. In section 4b, we further probe dynamic changes using the mixing length scale, hydrological cycling rate, and participation ratio, finding that the slowdown of the LHC seen in L17 for the wet component extends to the dry component and that changing subtropical dynamics drive an asymmetric response in the mixing length between the wet and dry components. In section 4c, we examine moist intrusions that transport moisture but do not participate in the LHC, with implications for AR. Our results highlight the predominant role played by the large-scale circulation in determining the dynamical response, suggesting that constraining changes in the spatial distribution of hydrologic cycle extremes in the extratropics must begin with constraining the meridional shifts in the large-scale circulation.

2. LHC budget formalism

The LHC is founded upon displacements ("intrusions") of column-integrated water vapor (CWV) from a semi-Lagrangian, zonally symmetric background state. This background state is determined by conservatively "zonalizing" the zonally meandering CWV isosurfaces. Schematically, this is illustrated for the Northern Hemisphere in Fig. 1. For an individual contour (red line), this process can be conceptualized as determining the parallel (termed the *equivalent latitude*, thick black dashed line) which divides the contour into two regions of equal area, one region consisting of the poleward moist intrusions (shaded in aqua) and the other of the equatorward dry intrusions (shaded in tan). Equivalently, the surface area enclosed poleward of the equivalent latitude is equal to that enclosed poleward of the contour. This process is accomplished numerically by sorting and rearranging a gridded CWV field, taking proper steps to ensure conservation of mass. Repeating this process for every equivalent latitude yields the background state.

It bears repeating that the background state defined here is better constrained to the climate state than the zonal mean, for reasons similar to those argued by Huang and Nakamura (2016) in the context of potential vorticity. Given this background state for CWV, we can now utilize it to define moist and dry intrusions and to integrate the net precipitation or evaporation within the moist and dry intrusions, defining the LHC.

To formally derive the LHC budget, we begin with the column water vapor equation, which can be derived by taking the vertical integral of the familiar moisture equation (see L17 or Trenberth and Guillemot 1995):

$$\frac{\partial m}{\partial t} = (E - P) - \nabla \cdot (m\mathbf{v}) \ . \tag{1}$$

Here m is column water vapor (CWV), E is column evaporation rate, P is column precipitation rate, and $\mathbf{v}$ is the vertically integrated product of specific humidity and horizontal velocity normalized by the CWV. Since the velocity is weighted by specific humidity, $\mathbf{v}$ can be thought of as the lower-tropospheric-mean horizontal velocity. Due to data availability constraints, we approximate column evaporation rate E and precipitation rate P with their surface rates. This does not account for the possibility of "teleportation" of CWV where

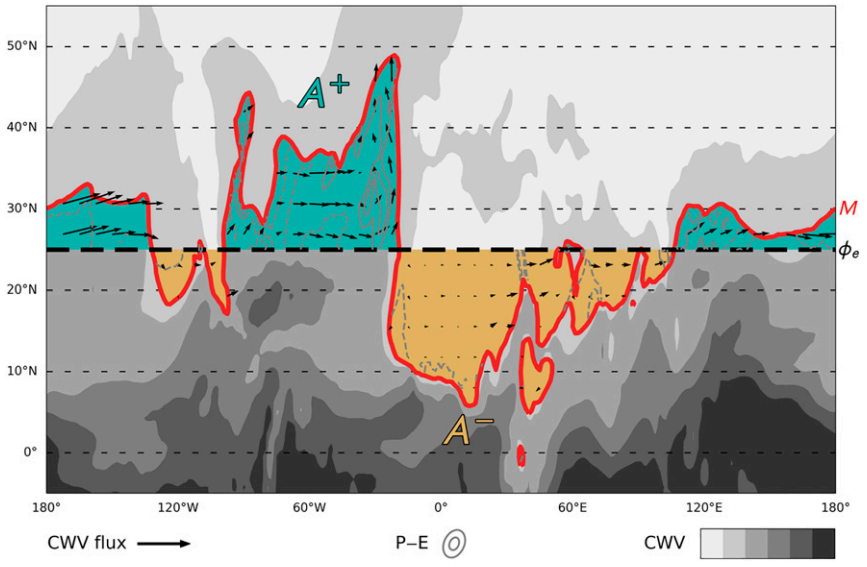

FIG. 1. Schematic of the wave activity transformation. Shading represents column water vapor (in 10 kg m^{-2} increments), arrows represent the moisture transport or column water vapor flux, and gray contour lines represent the net precipitation (in 3 mm day^{-1} increments). The thick black dashed line is the equivalent latitude, chosen such that the areas in tan and those in aqua have equal areas. Integrating net precipitation from the equivalent latitude to the red contour line at a particular longitude yields the local hydrologic cycle at that longitude and (equivalent) latitude.

water vapor is condensed, advected out of the column, and re-evaporated elsewhere, but we find these errors, in conjunction with model failure to conserve water mass, to be small, as in L17.

To focus on moist and dry intrusions and remove the background state, we utilize the local wave activity (LWA) transformation. LWA is a conservative line-integral transformation given by

$$\widetilde{(\,)} = \widetilde{(\,)}^{+} - \widetilde{(\,)}^{-} = \frac{a}{\cos\phi_e}\int_{m>M,\phi>\phi_e} (\,)\cos\phi\, d\phi - \frac{a}{\cos\phi_e}\int_{m<M,\phi<\phi_e} (\,)\cos\phi\, d\phi\,, \quad (2)$$

where a is the radius of Earth, ϕ is latitude, ϕ_e is the equivalent latitude, and M is the background state CWV; $\widetilde{(\,)}^{+}$ denotes integration over moist intrusions and $\widetilde{(\,)}^{-}$ denotes integration over dry intrusions. For further discussion of the LWA transformation, we refer the reader to the literature [in particular, L17, L18, and Xue et al. (2018), but also Huang and Nakamura (2016, 2017) and Nakamura and Solomon 2010, among others].

Applying the LWA transformation (2) to the CWV field yields the moist (A^+) and dry wave activity (A^-), which measure the amplitude of moist and dry intrusions, given by

$$A = A^{+} - A^{-} \equiv \widetilde{(m)}^{+} - \widetilde{(m)}^{-}. \quad (3)$$

We apply (2) to the full CWV field, instead of the more common choice for wave activities of the eddy field, as background state moisture still plays an important role in the generation of moist intrusions, as we will show. The CWV budget equation can be similarly transformed using LWA to produce the LHC budget. Changes in this budget will reveal changes that are driven by the background state M, which we term the "thermodynamic" component of the budget, and those that are driven by advective or overturning processes.

Integrating the CWV budget [Eq. (1)] using the definition of LWA [Eq.(2)] and of wave activity [Eq. (3)], and simplifying with the Leibniz integral rule, we yield the basic LHC budget:

$$\frac{\partial}{\partial t}(A - M\eta) = \widetilde{(E-P)} - \widetilde{[\nabla\cdot(m\mathbf{v})]}. \quad (4)$$

Here η represents the meridional extent of a moist intrusion or its mixing length, which will be discussed in more detail later. While further simplification of this budget will lead to greater insight, the basic budget has several important features. Most importantly,

$$\widetilde{(P-E)} \equiv \widetilde{(P-E)}^{+} + \widetilde{(E-P)}^{-} \quad (5)$$

represents the LHC, broken into wet and dry components (gray contours in Fig. 1). This definition reveals the LHC to be the net precipitation (evaporation) connected with moist (dry) intrusions, from processes such as warm conveyor belts, AR, low-level jets, or blocks. Since such events are frequently responsible for wet and dry extremes, the LHC agrees well with more traditional measures, such as the 99th percentile of $P - E$ (L18; Xue et al. 2018).

Equation (4) reveals that the LHC is balanced by the tendency of the adjusted wave activity ($A - M\eta$) and by the local moisture flux convergence (second term on the rhs, black arrows in Fig. 1). The wave activity must be adjusted because of our

choice to include the background state in our definition of wave activity, even though the background state itself does not drive the LHC. Importantly, the adjusted mean wave activity tendency is negligible on annual to decadal time scales because surface temperatures largely determine atmospheric moisture storage. This suggests that the dominant balance in (4) is between the LHC and the local moisture flux convergence; we will henceforth neglect the tendency. This introduces slight errors in the moist budget for the annual-mean and well-defined seasons and larger (but still small) errors in the dry budget and shoulder seasons (see Fig. 1 in the online supplemental material on the Journals Online website: https://doi.org/10.1175/JCLI-D-20-0780.s1).

To further simplify the basic budget (4) to gain further insight into the LHC, we partition m into a linear combination of the background state M and the intrusions, $m_e \equiv m - M$. We further apply Leibniz rule and split the horizontal velocity $\mathbf{v}$ into zonal u and meridional v components, aided by the integration of the moisture flux divergence $[\nabla \cdot (m\mathbf{v})]$ over a closed domain. This yields the following budget:

$$\widetilde{(P-E)} = -M\widetilde{(\nabla \cdot \mathbf{v})} + m_e v - \frac{\partial}{\partial x}\left[\widetilde{(m_e u)}\right]. \tag{6}$$

Here we use $\partial/\partial x \equiv [1/(a\cos\phi_e)]\partial/\partial\lambda$ (λ being longitude) for brevity. Equation (6) is developed more rigorously from (1) in section 1 of the online supplemental material.

Defining $\delta \equiv (6)_{\text{future}} - (6)_{\text{present}}$ as changes in (6) from present (1990–2005) to future (2071–80) climates, we decompose the annual-mean changes in the LHC budget:

$$\begin{aligned}\delta\widetilde{(P-E)} = &-(\delta M)\overline{\widetilde{(\nabla \cdot \mathbf{v})}} - \overline{M}\delta\left[\widetilde{(\nabla \cdot \mathbf{v})}\right] \\ &+ \delta(m_e v) - \delta\left\{\frac{\partial}{\partial x}\left[\widetilde{(m_e u)}\right]\right\}.\end{aligned} \tag{7}$$

Here the overbar $\overline{(\,)} \equiv 0.5[(\,)_{\text{future}} + (\,)_{\text{present}}]$ signifies the mean over both climates. In deriving (7), we neglect the cross term $\delta[M'(\widetilde{\nabla \cdot \mathbf{v}})']$ (primes indicate deviations from the time mean). This term varies primarily on seasonal time scales and does not change greatly between climate states (not shown). Thus, it represents a negligible fraction of the total annual and monthly changes. Ignoring this cross term means our decomposition tends to overpredict the magnitude of the changes mildly, but by less than 10% (see supplemental Fig. 1). Neglecting this term is not essential to our method nor does it impact our conclusions.

As a final step, the changes in the budget given in (7) are separated into moist and dry contributions, which is a unique advantage of this approach. Since moist intrusions (m_e^+) and dry intrusions (m_e^-) are computed separately, we can consequently apply this decomposition to moist and dry intrusions separately:

$$\delta\widetilde{(P-E)}^+ = -(\delta M)\overline{\widetilde{(\nabla \cdot \mathbf{v})}^+} - \overline{M}\delta\left[\widetilde{(\nabla \cdot \mathbf{v})}^+\right] + \delta(m_e^+ v) - \delta\left\{\frac{\partial}{\partial x}\left[\widetilde{(m_e u)}^+\right]\right\}, \tag{8a}$$

$$\delta\widetilde{(E-P)}^- = \underbrace{(\delta M)\overline{\widetilde{(\nabla \cdot \mathbf{v})}^-}}_{\text{thermodynamic}} + \underbrace{\overline{M}\delta\left[\widetilde{(\nabla \cdot \mathbf{v})}^-\right]}_{\text{overturning}} - \underbrace{\delta(m_e^- v)}_{\text{meridional advection}} + \underbrace{\delta\left\{\frac{\partial}{\partial x}\left[\widetilde{(m_e u)}^-\right]\right\}}_{\text{zonal LWA flux convergence}}. \tag{8b}$$

Each of the four terms on the rhs of (8) give some insight into what processes are physically responsible for modulating the LHC in a changing climate (see supplemental Fig. 2). The first term, $(\delta M)\overline{\widetilde{(\nabla \cdot \mathbf{v})}}$, represents the contributions from the increasingly moist background state M, weighted by the mean convergence (divergence); it therefore captures the dominant thermodynamic influences in the decomposition. The second term, $\overline{M}\delta\left[\widetilde{(\nabla \cdot \mathbf{v})}\right]$, quantifies contributions from changes in the low-level convergence of background moisture and is intimately linked to changes driven by a weakening overturning circulation (Held and Soden 2006; Vecchi and Soden 2007) and increasing static stability (Kang and Lu 2012; He and Soden 2017). The third term, $\delta(m_e v)$, corresponds to changes driven by meridional advection of moist or dry intrusions. It captures the primary contributions of phenomena that transport large amounts of moisture or dryness meridionally, such as AR and cyclones (tropical or extratropical) in the moist case, or anticyclones in the dry case. The final dynamic term, $\delta\{\partial/\partial x\left[\widetilde{(m_e u)}\right]\}$, is the zonal local wave activity (LWA) flux convergence and consists of changes in zonal variations in the zonal transport of moist or dry intrusions, which are prominent in jet-entrance, jet-exit, and coastal regions. By construction, the zonal LWA flux convergence term does not contribute to changes in the zonal-mean LHC (see L17). Given the predominantly rotational nature of the low-level extratropical flow, the zonal LWA flux convergence term largely offsets the meridional advection term. In designating contributions as "advective" (meridional advection and zonal LWA flux convergence terms) or "overturning," we note that these are not orthogonal like the result of a Helmholtz decomposition; rather, they reflect the dominant circulation regimes responsible for the resulting precipitation or evaporation.

Because the background state M is so fundamental to understanding the LHC and it drives the thermodynamic contributions, we argue here why it is expected to follow CC scaling under climate change. To begin, we define CWV saturation fraction $\sigma \equiv M/M_s$, where M_s is the saturation background state CWV, the temperature-controlled upper bound on the background state CWV. To first order, we assume that saturation CWV M_s responds to column temperature changes in the same fashion as saturation specific humidity (e.g., Lorenz and DeWeaver 2007). Denoting mass-weighted, vertically averaged $\langle\cdot\rangle$, CWV contour-following $\widetilde{(\cdot)}$ temperature as $\langle\tilde{T}\rangle$, this implies that $M_s \sim M_0 \exp[-L_v(R_{WV}\langle\tilde{T}\rangle)^{-1}]$, where M_0 is an unimportant

baseline constant for M_s. Thus, we expect the background state to behave as

$$M \sim \sigma M_0 \exp[-L_v(R_{WV}\langle\tilde{T}\rangle)^{-1}]. \quad (9)$$

We now divide future state (subscript 2) by present state (subscript 1) and assume the column saturation fraction does not change greatly between climate states (similar to the assumption of constant relative humidity, e.g., Held and Soden 2000). This assumption works reasonably well in most regions, which we will validate in section 4b. We also replace the vertically averaged temperature with the surface temperature since it is mass-weighted. This gives

$$\frac{M_2}{M_1} \sim \exp(\alpha \Delta \widetilde{T}_s), \quad (10)$$

where $\alpha \approx L_v R_{WV}^{-1} (\widetilde{T_s})^{-2}$, which should be roughly constant between climate states. Therefore, we expect changes in background zonal-mean CWV to scale in accordance with the CC relation as $\Delta(\ln M) \sim \alpha \Delta \widetilde{T}_s$ (cf. Lorenz and DeWeaver 2007; O'Gorman and Muller 2010).

3. Data and methods

To analyze the LHC response to climate change, we utilize archived data from the Community Earth System Model, version 1 (CESM) Large Ensemble (LENS). Briefly, CESM LENS is an approximately 1.25° × 1° coupled Earth system model simulation comprising 40 members started with varying initial conditions. A detailed description of the CESM LENS experiments is outlined in Kay et al. (2014). Six-hourly data including precipitation, latent heat flux, surface temperature, specific humidity, velocity, surface pressure, and surface geopotential height were downloaded from the National Center for Atmospheric Research. Having 40 ensemble members increases the ability to reduce internal climate variability, allowing for clearer identification of the forced response and of uncertainty related to internal variability. In this case, the response is forced by RCP8.5, the high emissions pathway that would result in a global radiative forcing of 8.5 W m^{-2} by 2100.

From the downloaded data, we compute CWV and CWV-weighted velocity according to L17 [see their Eq. (2)], and then apply the wave activity transformation (2) at each grid point for the Eulerian-equivalent terms in (8). Lagrangian quantities such as m_e cannot be properly handled by the numerical routine, and thus we use the equivalence $(\partial/\partial x)[\widetilde{(m_e u)}] \equiv (\partial/\partial x)[\widetilde{(mu)}] - M(\partial/\partial x)[\widetilde{(u)}]$ to diagnose the zonal convergence term.

The result of the wave activity transformation is that data appear at their equivalent latitude rather than their actual latitude. Since CWV increases moving equatorward, the equivalent latitude for moist wave activity is equatorward of its actual latitude and vice versa for the dry wave activity. This produces some artifacts, with a "squeezing" of the moist LHC at the equator and of the dry LHC at the poles. However, we do not correct for this because there is not a one-to-one mapping between the actual latitude of precipitation and its equivalent latitude. Nevertheless, as argued by L17 (see their Fig. 3), the vast majority of intrusions are within 5° of their equivalent latitude and the resulting center of precipitation is typically within 10°. The displacement between the precipitation center and the equivalent latitude is greatest in the subtropics, where the moisture transport function dominates the condensation function.

Further artifacts are introduced in the dry LHC budget by orography, which appears as a dry "island" with an equivalent latitude near the poles. Since these artifacts are local to orography, we mask all parts of the LHC (moist and dry) whenever the surface exceeds 800 m in height, and we mask poleward of the Himalayan Plateau for the dry LHC. While some proposals exist to correct for these artifacts, they are prohibitively computationally expensive and thus are left for implementation in future work.

4. Results and discussion

a. Processes behind hydrologic cycle change

The present-day (1990–2005) climatology of the wet LHC (Fig. 2a) in CESM LENS highlights regions of heavy precipitation, particularly emphasizing regions upstream of large moisture transport (black arrows), storm tracks, and the intertropical convergence zone (ITCZ). The good agreement between the low-level circulation and the spatial distribution of the LHC gives confidence that the nonlocality discussed in section 3 is generally small. Examining RCP8.5 fractional changes (2071–80 minus 1990–2005, divided by 1990–2005) in the wet LHC (Fig. 2b), we see a spatial pattern analogous to the wet-gets-wetter, dry-gets-drier pattern previously found for hydrologic cycle change (e.g., Held and Soden 2006). Fractional changes show decreases in the subtropics, where the present day is near zero; modest increases in the extratropics (with a notable local maximum in the North Atlantic, to be discussed in more detail later), where the LHC is largest in the present day; and only faint increases in the deep tropics. The latter result should be understood primarily as a consequence of the LWA transformation, which leads to a "squeezing" of Eulerian features near the equator and a small discontinuity at the equator itself.

There are two important results seen in the fractional change of the wet LHC. First, while the wet LHC tends to increase where it is wet and decrease where it is dry, the fractional changes shown here stray from the scaling of Held and Soden (2006), which predicts fractional changes that mirror surface temperature changes. The breakdown of this scaling for the LHC is consistent with the breakdown seen for the Eulerian zonally anomalous hydrologic cycle, where stationary eddy contributions generally show a spatial pattern of expansion rather than thermodynamic intensification (Wills et al. 2016). The other important result seen in these changes is the relatively good agreement between ensemble members (indicated by lack of stippling in Fig. 2b, which measures ensemble *disagreement*). The ensemble disagreement in future wet LHC changes is primarily seen on the edges of subtropical dry zones, suggesting that the disagreement may primarily be on the extent of subtropical expansion.

As might be anticipated, the climatology of the dry LHC (Fig. 2c) stands out in the subtropics and over major ocean evaporation basins, with subtropical stationary circulations

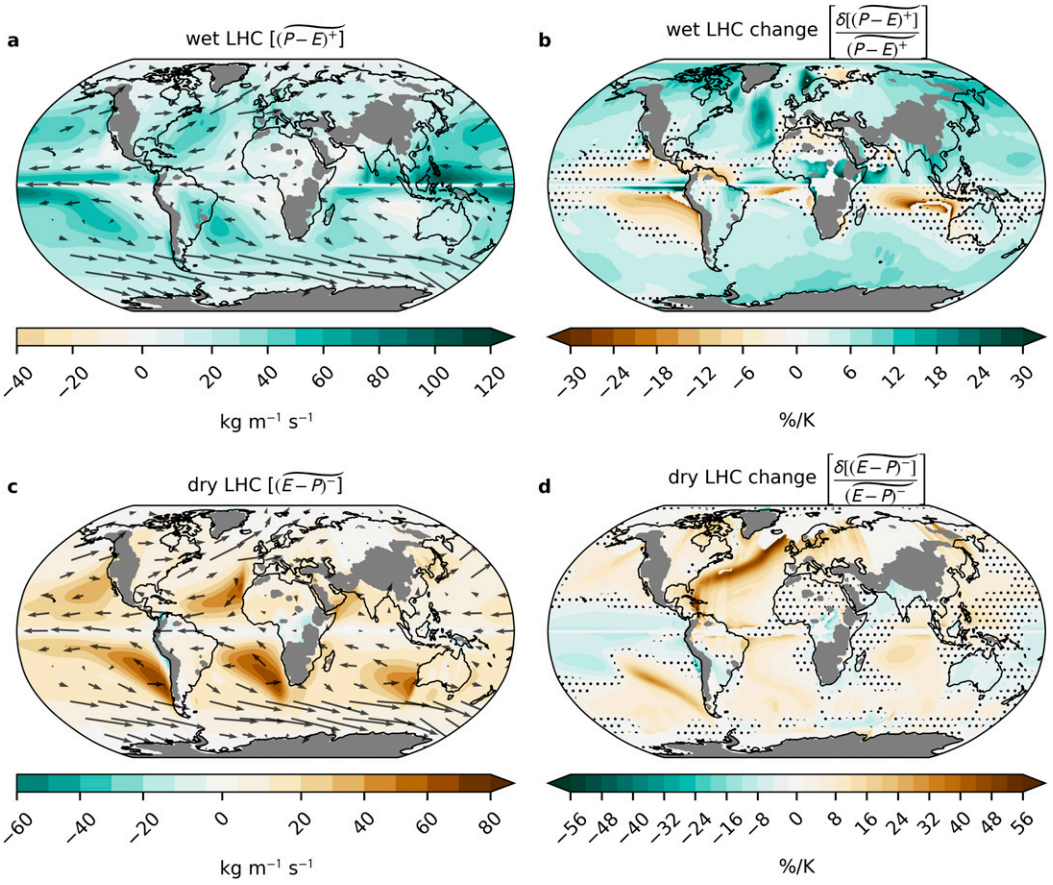

FIG. 2. Annual, ensemble-mean (a) present-day (1990–2005) wet local hydrologic cycle [LHC; $\widetilde{(P-E)}^+$; shading], (b) RCP8.5 (2071–80) fractional change in the wet LHC, (c) present-day dry LHC [$\widetilde{(E-P)}^-$; shading], (d) RCP8.5 fractional change in the dry LHC. Arrows in (a) and (c) represent the annual-mean, ensemble-mean, vertically integrated, specific-humidity-weighted velocity (**v**), a measure of low-level tropospheric flow. All data are taken from the CESMv1 Large Ensemble (LENS). Stippling represents regions where fewer than 85% of the 40 ensemble members agree on the sign of the response; land surface height above 800 m is masked in gray due to the impacts of orography on computing the LHC.

(black arrows) strongly influencing the spatial distribution. It is small over the land surface, likely due to soil moisture limiting evaporation. RCP8.5 fractional changes in the dry LHC (Fig. 2d) reveal the poleward expansion of the subtropical dry zones alongside a robust increase in most regions for evaporation connected with dry intrusions, with some modest weakening in the equatorial Pacific and over some land regions. Despite robust increases in the dry LHC, many of these regions also exhibit increases in the wet LHC, highlighting the compensating effects of hydrologic cycle intensification. These changes in the dry LHC further suggest that a simple thermodynamic scaling such as the dry-gets-drier paradigm does not adequately explain LHC changes. They also foreshadow the consistent storyline of this work that the subtropical expansion and precipitation decline has profound impacts on the wet and dry ends of the LHC.

We now diagnose the components of the LHC and its changes using (8). The spatial pattern of the present-day wet LHC is broadly set by the large-scale convergence of background moisture [$M\widetilde{(\nabla\cdot\mathbf{v})}^+$; Fig. 3a], which is strongest near the ITCZ but also contributes on the equatorward flank of storm track regions, reflecting the influence of overturning circulations. Meridional advection of moist intrusions (m_e^+v; Fig. 3c) tends to have local maxima in storm track regions, reflecting the importance of moisture transport for these regions. As expected, a portion of this meridional advection is offset by the zonal moist local wave activity (LWA) flux convergence, namely $\partial/\partial x[\widetilde{(m_e u)}^+]$ (Fig. 3e).

As with the moist case, the spatial structure of the present-day dry LHC is set by the spatial pattern of divergence of background moisture [$M\widetilde{(\nabla\cdot\mathbf{v})}^-$; Fig. 3b], which is connected with large-scale overturning. It is largest in the subtropics, with negative values (green shading) likely being artifacts of orography. Meridional advection of dry anomalies (m_e^-v; Fig. 3d) also exhibit local maxima in the subtropics and equatorward of storm tracks in regions of anticyclonic wave breaking. As before, the zonal divergence of dry LWA ($\delta\{\partial/\partial x[\widetilde{(m_e u)}^-]\}$; Fig. 3f) offsets some of the meridional advection.

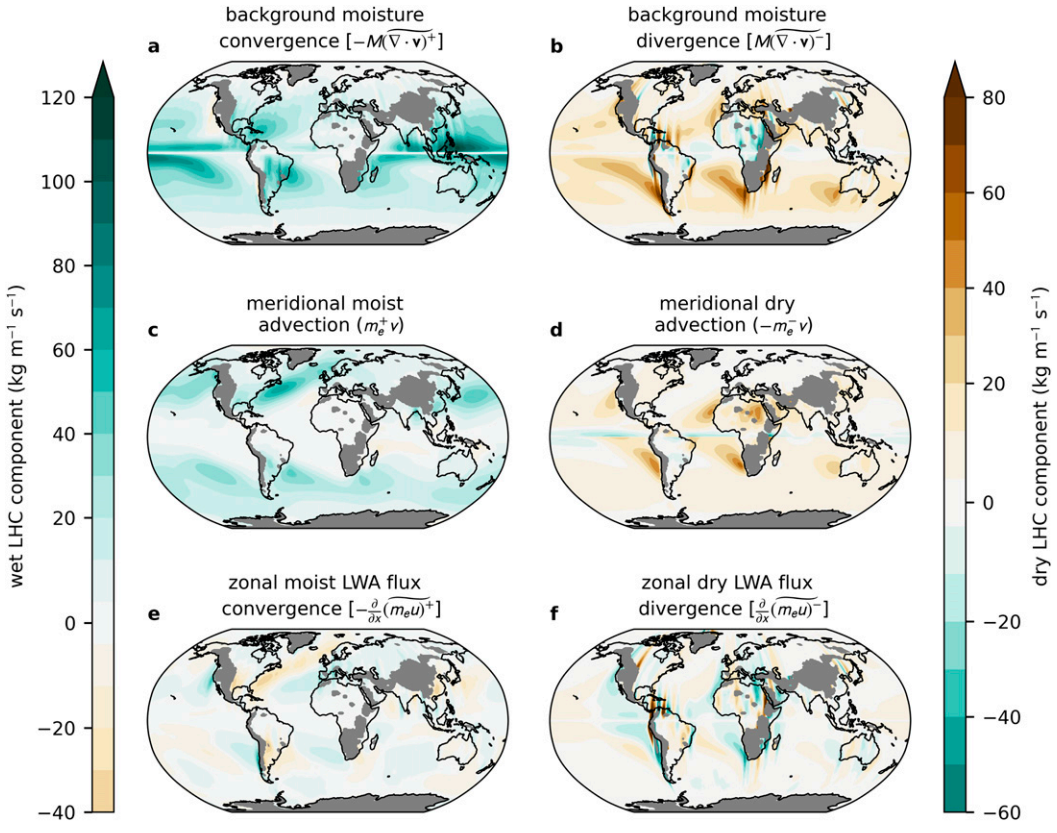

FIG. 3. Annual, ensemble-mean components of the closed LHC budget for the present-day (1990–2005) climate in CESM LENS. The LHC is balanced by the low-level (a) convergence or (b) divergence of background moisture, meridional advection of (c) moist or (d) dry intrusions, and the zonal (e) moist local wave activity (LWA) flux convergence or (f) dry LWA flux divergence. As in the previous figure, land surface above 800 m is masked (gray shading).

The results of this decomposition into overturning and advective components show that our budget-based decomposition can identify contributions to the LHC based on their associated circulation regime. While it is not unique in this capacity (e.g., Seager and Henderson 2013; Chen et al. 2019), our decomposition is rooted in the processes that produce or suppress precipitation and thus provides a new perspective to link changes in the circulation to the hydrologic cycle. To begin, we apply (8), normalized by the present-day LHC, to yield the RCP8.5 fractional changes. The "thermodynamic" contributions, $(\delta M)\overline{(\nabla\cdot\mathbf{v})}$, behave similarly between wet and dry budgets and agree with CC scaling in most regions (Figs. 4a,b). The addition of the convergence weighting $\overline{(\nabla\cdot\mathbf{v})}$ does lead to some zonal variations from CC scaling, particularly for the moist case. The dry thermodynamic response is largely positive, even with increasing background CWV, partially because an increase in water vapor holding capacity increases both vapor pressure deficit and the local slope of the CC relation, strengthening evaporation (Scheff and Frierson 2014).

Examining the contributors beyond the background state, we see that overturning contributions to the wet LHC ($\overline{M}\delta[\overline{(\nabla\cdot\mathbf{v})}^+]$; Fig. 4c) weaken it; possibly due to the weakening in the overturning circulation (Vecchi and Soden 2007) or the increase in dry static stability (Kang and Lu 2012; He and Soden 2017) suppressing large-scale convection. Overturning contributions to the dry LHC ($\overline{M}\delta[\overline{(\nabla\cdot\mathbf{v})}^-]$; Fig. 4d) dominate the structure of changing dry intrusions, with prominent suppression of dry intrusions (green shading) in most regions, particularly the equatorial Pacific. Despite the importance of weakening divergence for enhancing the dry LHC, it remains unclear whether this weakening is due to the increase in the effective dry stability and subsequent weakening of downward motion in a warming climate (Tamarin-Brodsky and Hadas 2019), the weakening of tropical large-scale overturning and its associated subsidence (Vecchi and Soden 2007), the weakening of radiatively driven subsidence by the longwave effects of increased greenhouse gases (Bony et al. 2013), or some combination of the above. Amidst this suppression, overturning contributions in the North Atlantic region act to enhance the dry LHC. One possible interpretation here is an expansion of subtropical dry zones and the poleward shift of storm tracks, both of which may allow for deeper propagation of dry waves into the midlatitudes.

Turning to contributions from advective circulations, meridional moist advection [$\delta(m_e^+v)$; Fig. 4e] dominates dynamic wet LHC changes in the midlatitudes, particularly in storm

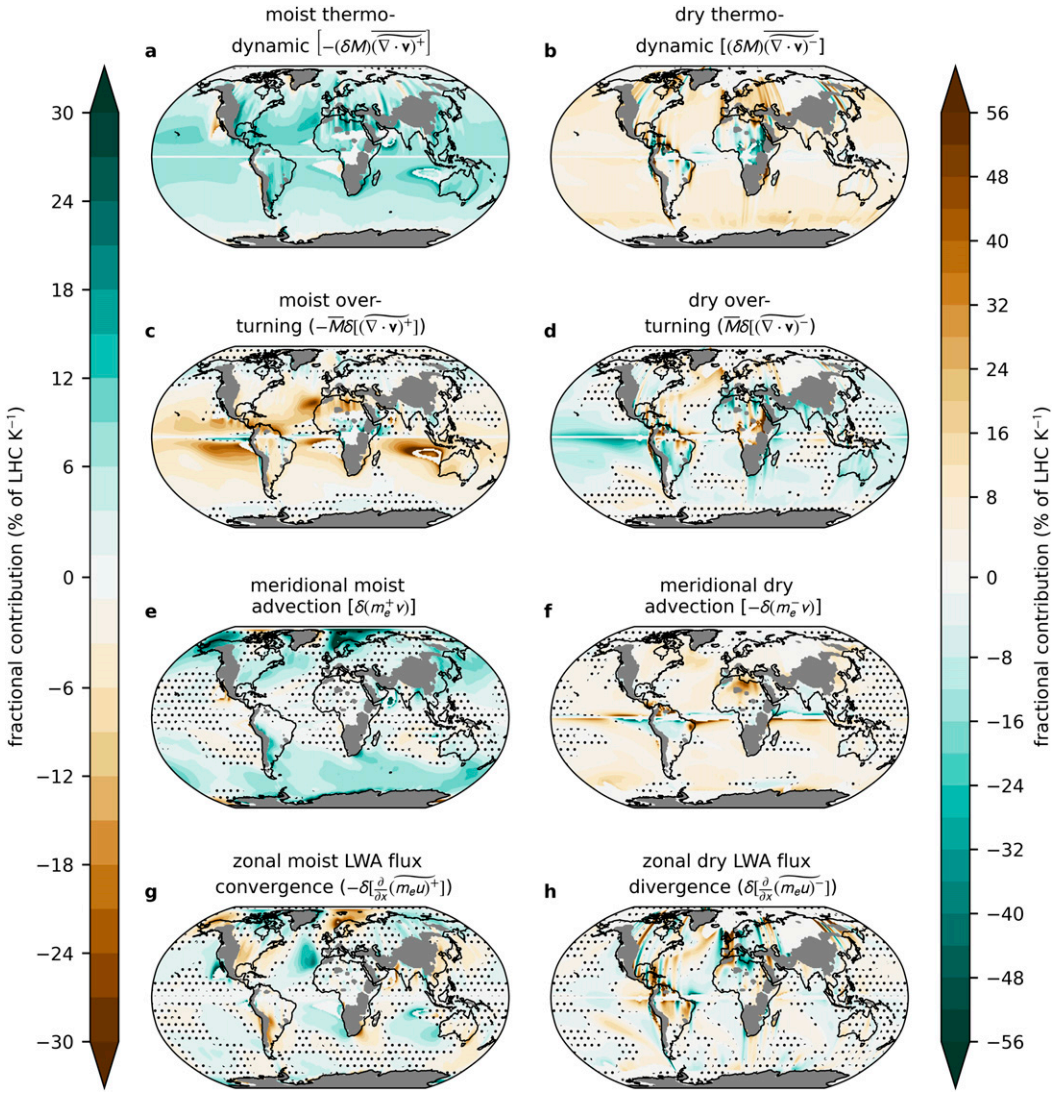

FIG. 4. Fractional contributions of the different components of the LHC to the fractional RCP8.5 change (2071–80 minus 1990–2005) in CESM LENS. Changes in the LHC are separated into those driven (a),(b) thermodynamically, (c),(d) by the overturning circulation, by the meridional advection of (e) moist or (f) dry intrusions, and by the zonal (g) moist LWA convergence or (h) dry LWA divergence. Contributions are determined by taking the change in each budget term of Eq. (8) and dividing by the present-day wet or dry LHC so that they remain additive. Stippling represents regions where fewer than 85% of the 40 ensemble members agree on the sign of the response. As in previous figures, land surface above 800 m is masked (gray shading). Note the differing scales between (left) wet and (right) dry LHC changes, chosen to align with Figs. 1b and 1d, respectively.

track regions, as expected. Close comparison of the changes with present-day contributions (Fig. 3c) reveals a modest poleward shift and intensification. This poleward shift is consistent with previous work (Chang et al. 2012; Tamarin-Brodsky and Kaspi 2017), although some studies, even those specifically examining CESM LENS, do not see dynamic intensification (Wang et al. 2017; Peings et al. 2017; Yettella and Kay 2017). In part, this difference could be due to the nature of the LHC compared to Eulerian metrics, as the former emphasizes the area of an intrusion and the latter emphasizes its temporal variance (Chang et al. 2012). Supporting this interpretation, Lagrangian compositing of extratropical cyclones in CESM LENS has shown that individual storms produce more precipitation, while their frequency and lifetime get reduced (Yettella and Kay 2017). This difference also foreshadows the residual thermodynamic influences in the advective term, which will be further discussed in section 4b.

Changes in meridional dry advection $[\delta(m_e^- v)$; Fig. 4f] are generally a weak but positive (drying) contributor to the dry LHC. The relative zonal homogeneity here suggests it may reflect the thermodynamic contributions of an increasing background moisture gradient. An important exception here is

near North Africa and the Mediterranean, where there is a local maximum in dry advection contributions that is largely offset by other changes.

The zonal moist LWA flux convergence ($\delta\{(\partial/\partial x)[\widetilde{(m_e u)}^+]\}$; Fig. 4g) is responsible for much of the heterogeneity of the wet LHC response. This term contributes positively (wetting) on the western boundary of continental landmasses, particularly over the western coast of the United States, both in the annual mean (Fig. 3g) and in DJF (not shown here). Because zonal LWA flux convergence can be generated by landfalling AR, increases of AR along the North American Pacific coast (Gao et al. 2015; Hagos et al. 2016; L18) may explain the increases seen here. Orography generally enhances this flux convergence on its windward (western; cf. Fig. 2a) side and suppresses it on the leeward (eastern) side, although some influence of orographic artifacts (as discussed in section 3) cannot be ruled out. There is a local maximum in contributions from the flux convergence in the jet exit region of the North Atlantic. This could be attributable to the cooler sea surface temperatures (SST) resulting from the North Atlantic warming hole (Menary and Wood 2018), which could trigger condensation for relatively warmer parcels zonally advected into the region.

The dry zonal LWA flux divergence ($\delta\{(\partial/\partial x)[\widetilde{(m_e u)}^-]\}$; Fig. 4h) is a crucial avenue for subtropical expansion of the dry LHC, particularly in the North Atlantic and South Pacific where subtropical anticyclones strengthen (He et al. 2017). Consistent with Scheff and Frierson (2012), who suggest that uncertainty in extratropical precipitation change predominantly results from subtropical expansion, we find this flux divergence term to be more uncertain (i.e., more stippling) than the other LHC contributors. Intriguingly, the zonal divergence appears to play a larger role than the meridional advection in determining the spatial structure of dry LHC changes. This suggests that an increase in the magnitude of dry intrusions (m_e^-, which appears in both advective terms) is not sufficient to explain the advective changes. This is significant because m_e is partly thermodynamic, as we now explain.

b. Isolating dynamic changes

Because advective terms are influenced by a steepening moisture gradient, they do not represent purely "dynamic" contributions to the LHC. While these budget terms do not explicitly contain the background state M, a simple diffusive picture (e.g., Vallis 2006; Caballero and Hanley 2012) of a moist or dry intrusion suggests that its magnitude [$m_e \sim (\partial M/\partial y)\eta$] depends on its mixing length (η) and the gradient ($\partial M/\partial y$) it is mixed across. Changes in this gradient are essentially a thermodynamic response given the exponential response of the background state (i.e., CC scaling; also see Caballero and Hanley 2012).

To demonstrate that the background gradient obeys CC scaling like the background state, we derive a scaling for it by taking the meridional gradient of (9) and taking the ratio between future and present climate states, as before. We also neglect terms that do not contribute in the first order. The result, derived more rigorously in section 2 in the online supplemental material (on the Journals Online website: https://doi.org/10.1175/JCLI-D-20-0780.s1), is

$$\frac{\dfrac{\partial M_2}{\partial y}}{\dfrac{\partial M_1}{\partial y}} \sim \frac{\dfrac{\partial \widetilde{T_{s,2}}}{\partial y}}{\dfrac{\partial \widetilde{T_{s,1}}}{\partial y}} \exp(\alpha \Delta \widetilde{T_s}). \tag{11}$$

Thus, to more cleanly separate thermodynamic from dynamic influences on the LHC, we introduce the LHC scaling. This scaling is independent of the budget analysis of section 4a and derives from the semiempirical linear relationship between wet (dry) LHC and moist (dry) wave activity. This relationship, found for the moist and total wave activities by L17 and L18, also extends to the dry, and it is expressed as

$$\widetilde{(P-E)}^+ \sim \frac{A^+ - A_c^+}{\tau^+}, \tag{12a}$$

$$\widetilde{(E-P)}^- \sim \frac{A^-}{\tau^-}. \tag{12b}$$

Here A_c^+ is the critical amplitude (supplemental Fig. 4), defined as the minimum amplitude required of a moist intrusion to participate in the wet LHC. It is calculated as the intercept in the linear regression between A^+ and $(P-E)^+$ (L17; Xue et al. 2018). The intercept is negligible for the dry regression, implying that dry waves do not need a critical amplitude. (This asymmetry is analogous to ascent and descent, the latter always being unsaturated.) The other important scaling factor here is τ, which represents the time scale over which moist and dry intrusions are damped by their respective sinks (supplemental Fig. 4). Since the LHC acts as a wave activity forcing on short time scales [$\partial A/\partial t$; see (4)], τ can be understood as an approximate e-folding relaxation time for the wet LHC to return wave activity to its critical amplitude and the dry LHC to return wave activity to the background state.

When calculating the above regression, we first aggregate the 1.25° × ~1° data into 7.5° × ~6° data (using six-by-six blocks of the original grid as the new grid cell) because the strength of the linear relationship between A and $\widetilde{(E-P)}$ comes in part from the central limit theorem (L17). For most grid cells, this brings enough "normality" to justify the linear regression; aggregating over larger areas does not substantially improve performance (not shown). Because the choice of independent variable in the regression is arbitrary, we utilize reduced major-axis regression (see L17 and references therein). When displaying the time scale and critical amplitude, we interpolate back to the original 1.25° × 1° grid for consistency with the mixing length.

To remove the thermodynamic effects of the moisture gradient, the wave activity in (12) can be scaled like a wave amplitude as $A^+ \sim m_e^+ \eta^+ \sim (\partial M/\partial y)(\eta^+)^2$ or $A^- \sim m_e^- \eta^- \sim (\partial M/\partial y)(\eta^-)^2$ (L17), where η is the mixing length. Combining this with (12) yields the scaling for the wet or dry LHC:

$$\widetilde{(P-E)}^+ \sim \frac{\partial M}{\partial y}\frac{A^+ - A_c^+}{A^+}\frac{(\eta^+)^2}{\tau^+}, \tag{13a}$$

$$\widetilde{(E-P)}^- \sim \frac{\partial M}{\partial y}\frac{(\eta^-)^2}{\tau^-}, \tag{13b}$$

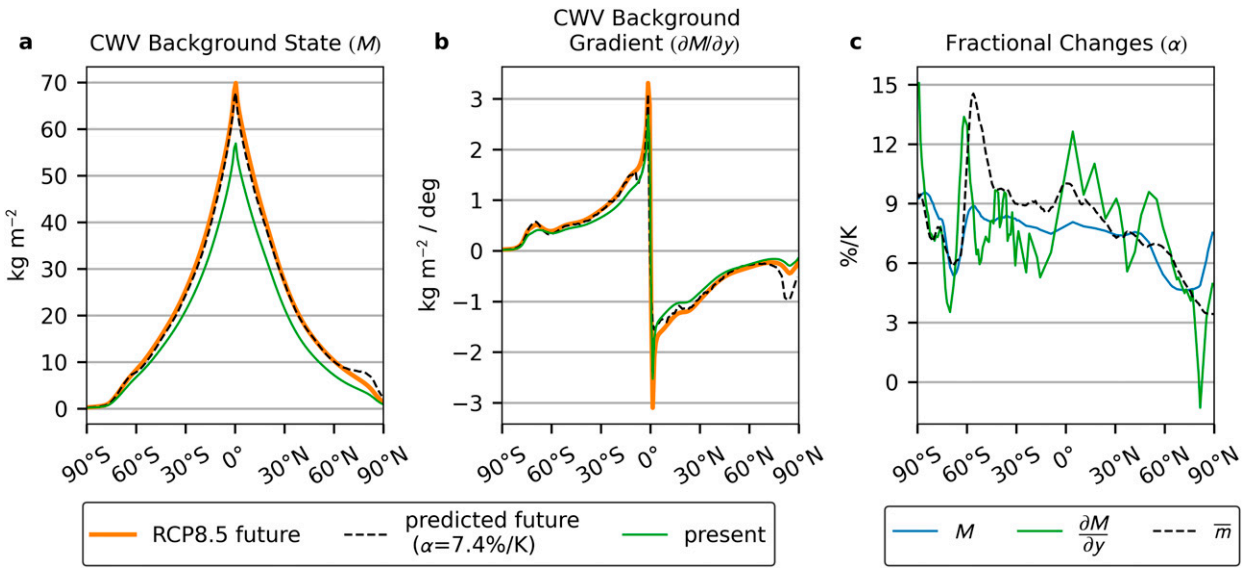

FIG. 5. Using an $\alpha = 7.4\%\ \mathrm{K}^{-1}$ (O'Gorman and Muller 2010; Lorenz and DeWeaver 2007), we are able to predict the future distribution of (a) the column water vapor (CWV) background state M and (b) its meridional gradient $\partial M/\partial y$ given the present state and the RCP8.5 change (2071–80 minus 1990–2005) in zonal-mean temperature in CESM LENS, utilizing (10) and (11). We also compute (c) the scaling factor α directly from RCP8.5 changes to assess where the theory holds well and to compare it to the zonal-mean CWV $\overline{m}$, which does not follow Clausius–Clapeyron scaling as strongly as the background state M.

or, in its fractional form:

$$\frac{\delta\widetilde{(P-E)}^{+}}{\widetilde{(P-E)}^{+}} \sim \frac{\delta\left(\dfrac{\partial M}{\partial y}\right)}{\dfrac{\partial M}{\partial y}} + 2\frac{\delta\eta^{+}}{\eta^{+}} + \frac{\delta(\tau^{+})^{-1}}{(\tau^{+})^{-1}} + \frac{\delta\left(\dfrac{A^{+}-A_c^{+}}{A^{+}}\right)}{\dfrac{A^{+}-A_c^{+}}{A^{+}}}, \tag{14a}$$

$$\frac{\delta\widetilde{(E-P)}^{-}}{\widetilde{(E-P)}^{-}} \sim \frac{\delta\left(\dfrac{\partial M}{\partial y}\right)}{\dfrac{\partial M}{\partial y}} + 2\frac{\delta\eta^{-}}{\eta^{-}} + \frac{\delta(\tau^{-})^{-1}}{(\tau^{-})^{-1}}. \tag{14b}$$

Intuitively, the scaling suggests changes in the wet and dry LHC are driven by 1) a changing background moisture gradient, 2) a changing mixing length scale, and 3) a changing cycling rate (τ^{-1}). In addition, the wet LHC (14a) may also be influenced by changes in the quantity $(A^{+} - A_c^{+})/A^{+}$, termed the participation ratio, which reflects the portion of a moist intrusion exceeding the critical amplitude and thus being damped by ("participating in") the wet LHC. Absent the participation ratio, the scaling in (13) has a similar form to other diffusive scalings of the eddy moisture flux (cf. Caballero and Hanley 2012), whose vertical integral largely balances precipitation.

The mixing length η we define here is thus qualitatively similar to Eulerian estimates as a measure of the effective displacement of column-mean moisture by large-scale eddies, which is related to the width of the baroclinically unstable zone (particularly for the moist mixing length). Crucially, however, the moist and dry mixing lengths measure displacement from the wave-free, conservatively estimated background state M rather than the zonal mean. Since the zonal-mean CWV decreases poleward more gradually than the background state, this generally results in a longer (but similar order of magnitude) estimate of mixing length compared to other estimates (cf. Caballero and Hanley 2012; Swanson and Pierrehumbert 1997; Tandon et al. 2018). Further, the adiabatic assumption that guides the construction of the background state (Nakamura and Solomon 2010) may result in longer mixing lengths than those accounting for strong diabatic effects (Caballero and Hanley 2012). Despite these differences in definition, the mixing length utilized for the LHC plays a large role in the magnitude and spatial distribution of the LHC's dynamic response since it is the only quadratic term in the scaling. Thus, it provides important insight into how large-scale moisture transport processes driven by eddy stirring can modify the LHC.

Before analyzing the dynamic changes in the LHC in detail, we first verify the thermodynamic scalings for the background state and gradient (Fig. 5). CWV background scaling is evaluated in Fig. 5a, where we use a slight modification of (10) to predict the future CWV background distribution (M_2) given the present-day quantities (subscript 1), present-day and RCP8.5 zonal-mean temperature, and an Earth-like $\alpha = 7.4\%\ \mathrm{K}^{-1}$ (O'Gorman and Muller 2010; Lorenz and DeWeaver 2007). We calculate the present-day CWV-associated temperature as the surface temperature along a CWV contour [$\widetilde{T}_s \equiv \widetilde{T}_s(\phi_e)$], and we approximate the future CWV-associated temperature by multiplying its present distribution with the ratio of the RCP8.5 to present-day zonal-mean

temperatures [$\widetilde{T_{s,2}} \approx \widetilde{T_{s,1}}(T_{s,2}/T_{s,1})$]. This ensures we are not unfairly utilizing the future CWV distribution to predict the background state CWV.

Overall, the scaling performs quite well for most latitudes for the background state (Fig. 5a), which monotonically decreases moving poleward by construction. The scaling modestly underpredicts the background CWV near the equator, where CWV-associated temperature is not well defined, and it overpredicts the background CWV in the Northern Hemisphere high latitudes. The scaling likely overpredicts here because the assumption of constant CWV saturation fraction (σ) holds less well over land than ocean (i.e., Byrne and O'Gorman 2015).

Despite the approximations required to compute gradients numerically on a coarse grid, we successfully predict the future gradient (Fig. 5b) using (11) in the same manner as we used (10) to predict the background state. This demonstrates that the sharpening moisture gradient is fundamentally a thermodynamic response. The gradient scaling also does not accurately predict changes near the equator (where the gradient is poorly defined) or in the high-latitude Northern Hemisphere, likely for the same reason the background state scaling overpredicts changes in this region.

Instead of using a fixed rate α to predict future changes, we also compute it directly to evaluate the degree to which RCP8.5 changes obey the CC relation. This "CC rate" is like a fractional rate of change except it accounts for the exponential scaling of the CC relation (O'Gorman and Muller 2010). It increases relatively uniformly, with most regions hovering around 7.5% K^{-1} (Fig. 5c). In contrast, the CC rate for Eulerian zonal-mean CWV is more variable with latitude (black dashed line). Thus, we argue that M is better constrained by CC scaling than its Eulerian counterpart and is an effective measure of thermodynamic impacts. The fractional changes in gradient fluctuate meridionally considerably more than the changes in the CWV background, but as we have shown the changes are essentially thermodynamic.

We proceed to use the LHC scaling to examine the LHC structure for the present-day annual mean (Fig. 6), beginning with the mixing length. The mixing length is calculated by directly computing the displacement of the M contour from its equivalent latitude. The present-day moist mixing length scale (Fig. 6a) is long on the equatorward flanks of storm tracks and in monsoon regions, reflecting how these circulations transport moisture, both directly and indirectly through enhanced wavebreaking. The dry mixing length scale is largest in the subtropics (Fig. 6b), as the large values poleward of orography are likely artifacts from the orographic "dry island" effect (see section 3). Interestingly, the dry mixing length scale exhibits local maxima over North Africa, the western United States, and Australia, while the dry LHC is generally small over land (Fig. 2b) due to the soil moisture constraint on evaporation.

The moist cycling rate (Fig. 6c) increases from very low values in the subtropics (long moist time scale) to high values in the polar regions (short moist time scale), especially near orography. In contrast, the dry cycling rate (Fig. 6d) is very low in the tropics, likely because upward motion in convective regions is stronger than downward motion (Bretherton et al. 2005) which leads to longer dry wave lifetimes. Both cycling rates tend to be strongest in the vicinity of storm tracks, particularly in jet entrance and exit regions, where wave breaking leads to mixing and brief wave lifetimes.

The present-day structure of the participation ratio (Fig. 6e) can be understood by considering the critical amplitude. In the tropics, where the critical amplitude is kept low by deep convection, the participation ratio is high. It decreases rapidly into the subtropics, where a large critical amplitude favors the transport of wave activity rather than its conversion into precipitation. This minimum participation ratio is critical for transport by AR, which is examined further in section 4c. Storm track regions also exhibit local maxima in the participation ratio, as the increased baroclinicity reduces the critical amplitude (Xue et al. 2018).

Now we use (14) to decompose RCP8.5 changes in the LHC. Overall, the cumulative scaling contributions match the spatial pattern of changes quite well, with some overestimation of their magnitude, particularly in the dry case (supplemental Fig. 3). Changes in mixing length scale (Figs. 7a,b) again paint a picture of dynamically driven drying in the subtropics and midlatitudes, with increases in dry length scale and decreases in moist length scale, consistent with the weakened midlatitude stirring found by L17. A notable exception to this is over the Southern Ocean and to an extent the North Pacific, consistent with projections of intensified storm tracks (Chang et al. 2012). Advective contributions to the LHC budget (Figs. 4e–h) support this notion. Comparing with climatology (Figs. 6a,b), length scale changes also suggest a poleward shift of storm tracks, which is more consistent with previous findings than the results from the budget-based decomposition.

Changes in the hydrological cycling rate portray an increasing residence time (decreasing rate) for moist waves (Fig. 7c; brown shading), consistent with but more general than the slowdown of the general circulation predicted by earlier work (e.g., Held and Soden 2006; Vecchi and Soden 2007). This result is consistent with L18, who attribute the change to a weakening of vertical motion or an upward shift of the atmospheric circulation (Singh and O'Gorman 2012). Likewise, residence times decrease for dry waves in almost all regions (Fig. 7d; green shading) except the deep tropics. A possible explanation for the decreasing lifetime for dry waves is the weakening of downward vertical motions by the increasing dry static stability (Tamarin-Brodsky and Hadas 2019).

The participation ratio (Fig. 7e) decreases in most regions (brown shading). This may be due to the increase in the atmospheric moisture storage capacity, which gives rise to a smaller fraction of moist waves which condense into precipitation. An important exception occurs near the North Atlantic warming hole. In this region, cooler SSTs lead to strong growth in moist wave damping and an increase in the LHC. This interpretation is supported by the large increases in the North Atlantic that are seen in the zonal moist LWA flux convergence (Fig. 4g). As a reference, the fractional change in moisture gradient from Fig. 5c is shown again (Fig. 7f), normalized by global-mean temperature, as it contributes positively toward both ends of the LHC.

c. *Implications for atmospheric rivers*

Beyond providing a clean separation between dynamic and thermodynamic components, this scaling can be further utilized

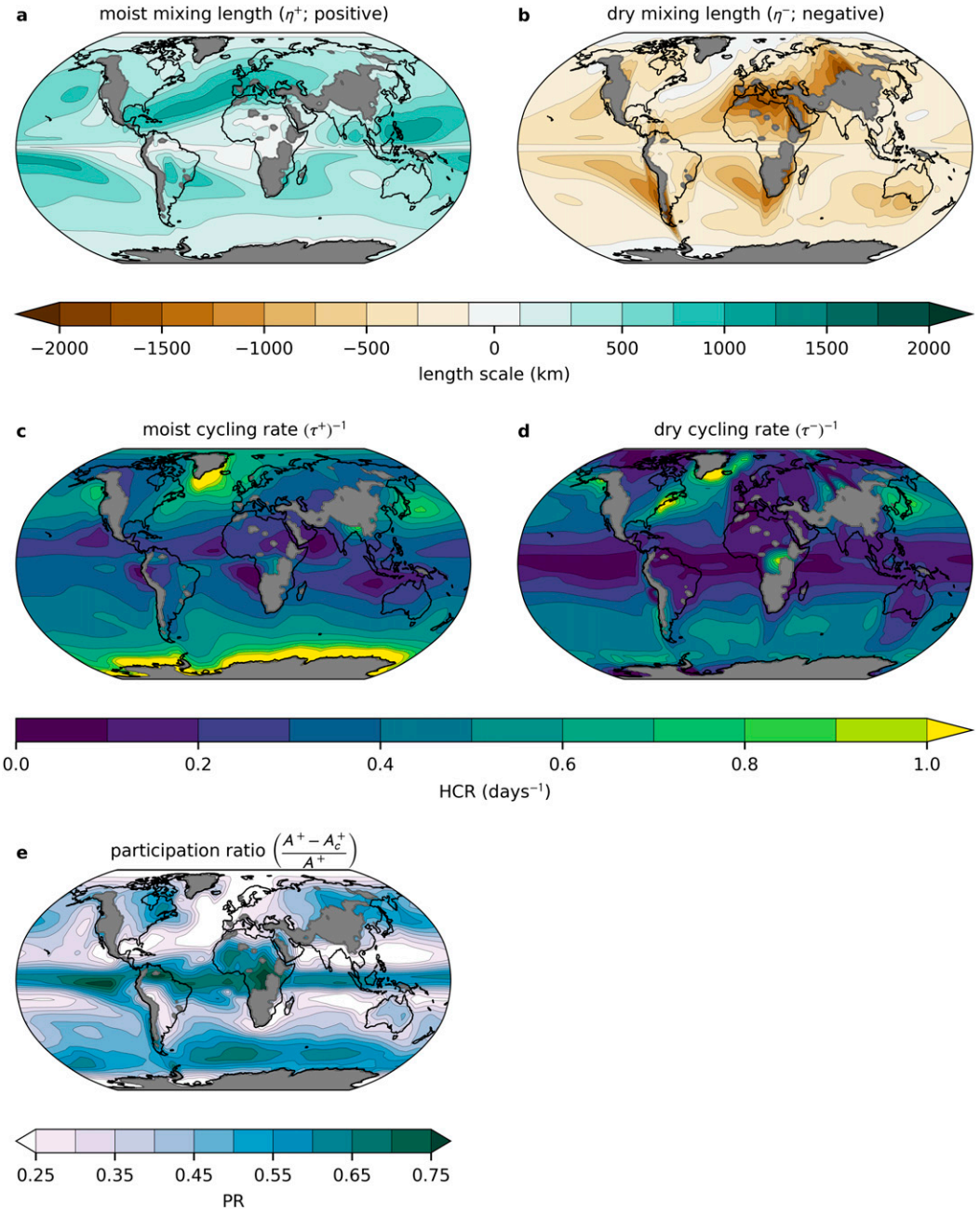

FIG. 6. Annual, ensemble-mean (a),(b) mixing length scales, (c),(d) cycling rates, and (e) participation ratio for the present-day (1990–2005) climate in CESM LENS. As in previous figures, land surface above 800 m is masked (gray shading).

to probe moisture transport, particularly by ARs. Crucially, the scaling reveals that a moist intrusion is not entirely available for participation in the wet LHC, as some proportion of it {measured by one minus the participation ratio, or $1 - [(A^+ - A_c^+)/A^+] \equiv A_c^+/A^+$} must be reserved due to energetic limitations and the temperature dependence of saturation. Thus, the critical amplitude A_c^+ measures the moisture transport by intrusions that does not result in precipitation. Because the nonprecipitating portions of ARs are characterized by large wave activity and low participation ratio (L17), A_c^+ has important implications for moisture transport by ARs. This picture of the wet LHC is akin to a watershed with a dam controlling its outlet (Fig. 8).

In this analogy, the moist wave activity measures the amount of water in the watershed. Any influx of water (wave activity) into the watershed that exceeds the capacity of the dam, which

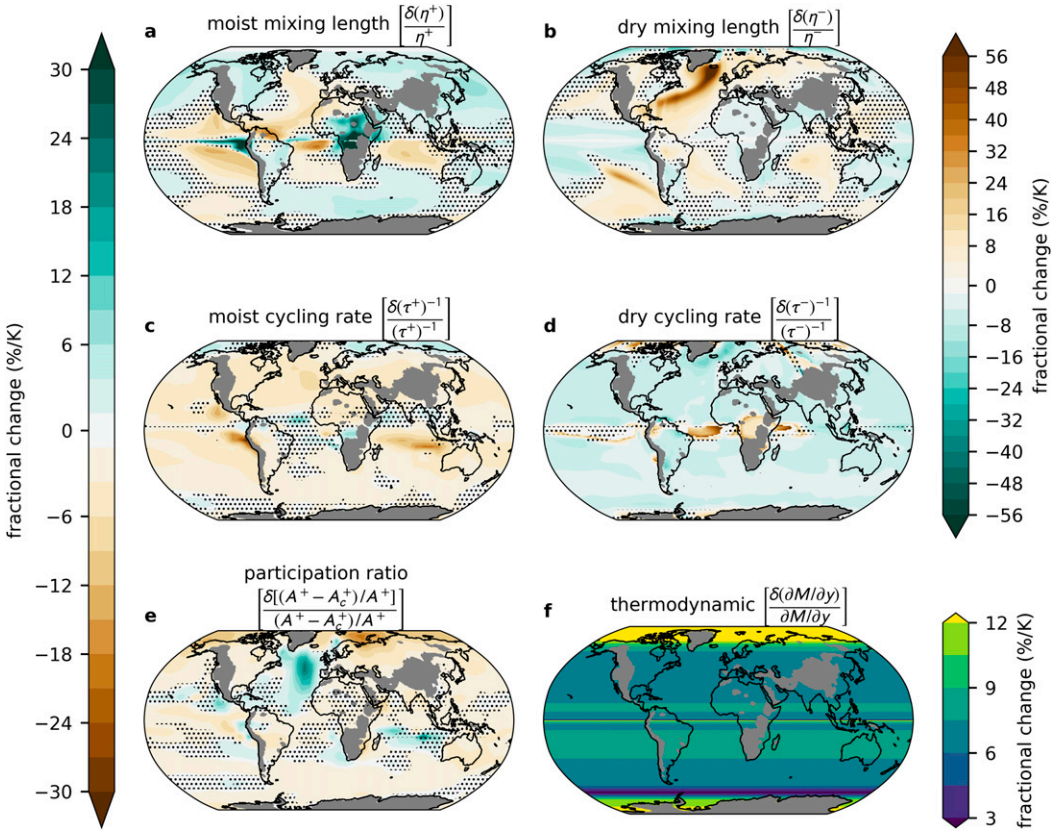

FIG. 7. Annual, ensemble-mean fractional RCP8.5 (2071–80 minus 1990–2005) changes for the (a) moist and (b) dry mixing length scale, (c) moist and (d) dry cycling rates, (e) wet LHC participation ratio, and (f) background moisture gradient in CESM LENS. Changes in the wet LHC consist of contributions from the background moisture gradient, moist mixing length (weighted double the other contributions), moist time scale, and the participation ratio. The dry LHC consists of similar contributions as the wet, except using the dry counterparts and excluding the participation ratio. Stippling represents regions where fewer than 85% of the 40 ensemble members agree on the sign. As in previous figures, land surface above 800 m is masked (gray shading). Note the different scales between wet and dry changes.

represents the critical amplitude, must be released from the watershed. This released fraction of the water constitutes the wet LHC, and the rate the dam releases water is the cycling rate. Just as an understanding of a watershed's outlet would be incomplete without examining the regulating reservoir, this analogy suggests that our understanding of the active LHC could be furthered by examining the critical amplitude.

To accomplish this, we utilize a scaling for the critical amplitude similar to the moist wave activity $A^+ \sim (\partial M/\partial y)(\eta^+)^2$:

$$A_c^+ \sim \frac{\partial M}{\partial y}(\eta_c^+)^2. \tag{15}$$

Here, η_c^+ takes on the meaning of "mean free path" or the distance moist waves can propagate with their humidity content conserved (L17). Thus, it resembles estimates of mixing length that rely on tracer conservation, such as meridional velocity autocorrelation (e.g., Swanson and Pierrehumbert 1997; Caballero and Hanley 2012). However, it is longer than these other estimates, just as the moist and dry mixing lengths were, and for the same reasons. Similarly to the mixing length, the mean free path represents the dynamic contribution to changes in the critical amplitude.

As previously mentioned, we calculate the critical amplitude as the intercept from the regression in (12a), and we subsequently use (15) to calculate the mean free path. The present-day critical amplitude in CESM LENS (Fig. 9a) highlights source regions for AR where moisture transport exceeds moisture loss via condensation, such as the western Pacific and North Atlantic, as we would expect. While ARs are not stationary like the reservoirs in our analogy, they are the dominant meridional moisture transporters (Zhu and Newell 1998) and are inefficient precipitators (L17; L18), making them the major contributors to the critical amplitude. However, the critical amplitude is not capturing AR impacts, as it is distinct from the LHC, which results in (net) precipitation.

Under RCP8.5, the critical amplitude (Fig. 9b) increases in a similar fashion to the wet LHC (Fig. 2b), except with smaller decreases in the subtropics and larger increases near the poles. Despite showing a strong increase in the wet LHC (Fig. 2b), the North Atlantic region shows a modest decrease in the reserved LHC, which may partially explain the increase in the active portion (if one assumes the total LHC does not change significantly in this region).

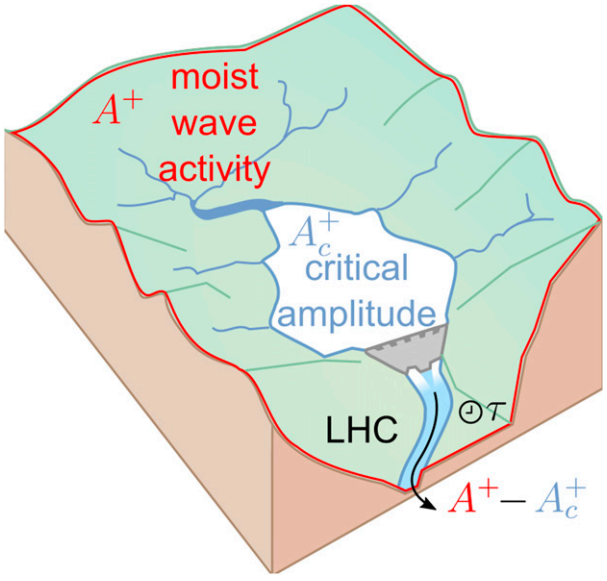

FIG. 8. Schematic illustrating the different components of the LHC framework, which is akin to a watershed with a dam or levy at its outlet.

The present-day mean free path (Fig. 9c) is longest in jet entrance and exit regions, illustrating how large-scale wave breaking transports moisture by stretching material contours and elongating the mean free path. The present-day mean free path is particularly large over the North Atlantic, where the strong, wintertime storm track excels at transporting moisture from near the subtropics into the Arctic (supplemental Fig. 5), and over the northern Indian Ocean and northwest Pacific, where summertime monsoonal circulations are the dominant moisture transporters (supplemental Fig. 6; Xue et al. 2018). The mean-free path is large over continental interiors during the summer season, perhaps reflective of the role of low-level jets (Algarra et al. 2019).

While the critical amplitude generally increases in a warmer climate, RCP8.5 changes in mean free path (Fig. 9d) show a decrease in subtropical regions and an increase in higher latitudes. A crucial exception to this high-latitude lengthening is in the North Atlantic near the warming hole. This unravels the dynamics behind the super-CC increase seen in the wet LHC here (Fig. 1b): the cooler SST act to enhance condensation, reduce the mean free path, lower the critical amplitude, and thereby raise the participation ratio (Fig. 7e), which is the central dynamic contributor. This is consistent with the previous budget-based results (Fig. 4g) that the warming hole results in a locally sharpened SST gradient, enhancing baroclinicity and the participation ratio, and also increasing the downstream convergence of moist wave activity.

Changes in mean free path (Fig. 9d) also explain the subtropical decreases in the critical amplitude (Fig. 9b), which is consistent with a weakened stirring (L17). Whether this decline will exceed the thermodynamically driven increase appears to underlie the ensemble uncertainty in critical amplitude (stippling, Fig. 9b). As with uncertainty in the moist mixing length (Fig. 7a), the uncertainty in mean free path (stippling, Fig. 9d) is largely at the margins of the subtropical decline, implicating the strength of the expansion as the source of uncertainty. This result further emphasizes the profound impacts of subtropical expansion on the LHC, suggesting that further insight into dynamic LHC changes should focus on the impacts of subtropical change on wave breaking and moisture transport.

5. Summary and conclusions

Here we have conducted a thorough analysis of changes in the local hydrologic cycle (LHC) for the RCP8.5 scenario as simulated by the CESM1 Large Ensemble (LENS). Our dynamical approach provides two independent methods for decomposing wet and dry LHC changes, with contributions either from overturning and advective circulations, or from the moisture gradient, mixing length, and cycling rate (and participation ratio for the moist case). We show the thermodynamic changes measured here are commensurate with the Clausius–Clapeyron relation. To the first order, changes in tropical LHC are due to thermodynamic increases countered by weakening low-level convergence, likely due to the slowdown of the Hadley circulation (Lu et al. 2007; Vecchi and Soden 2007) and increasing land–sea contrast (He and Soden 2017).

In the midlatitudes, wet LHC changes are driven by thermodynamic increases in conjunction with increasing meridional advection. This advection primarily results from extratropical cyclones and atmospheric rivers, pointing to the need for a robust understanding of midlatitude storm track changes. The dominant pattern of dry LHC changes is one of subtropical expansion. These changes are mainly driven by changes in overturning and in the zonal dry LWA flux divergence, the latter being key in jet entrance and exit regions.

Our scaling-based approach further reveals a global slowdown in the LHC cycling rate, along with a shortened moist mixing length but a lengthened dry mixing length for the midlatitudes. These changes appear linked to subtropical expansion and changes in stability, which also reduce the moisture mean free path.

Based on this analysis, we argue that the meridional shift and weakening of the general circulation is the predominant dynamic driver behind the intensifying LHC in CESM LENS. While we do not neglect the importance of different regionally relevant mechanisms, we can quantify their relative and synthetic contributions and directly link changes in the LHC to changes in different circulation regimes. This suggests that ongoing efforts to predict and constrain circulation changes may ultimately help constrain annual changes in the mean hydrologic cycle and the extremes (Shepherd 2014; Pfahl et al. 2017).

We now suggest several avenues for future work. The dry LHC budget analysis presented here is a unique contribution of this work, but the presence of strong artifacts over the land surface makes it difficult to interpret for many important regions. Future work should seek to minimize the numerical impacts of orography on the dry LHC. Changes in dryness are often considered on longer time scales than the 6-hourly changes analyzed here (Polade et al. 2014), which creates a challenge for contextualizing these results. Yet the changes in the dry LHC over the ocean modestly resemble the spatial patterns of change seen in changes in dry days (Polade et al. 2014), increasing our confidence in the relevance of these results.

Ongoing extension of this work will analyze CMIP6 models to identify the robust dynamic contributions to the LHC change under global warming and the dynamical sources of

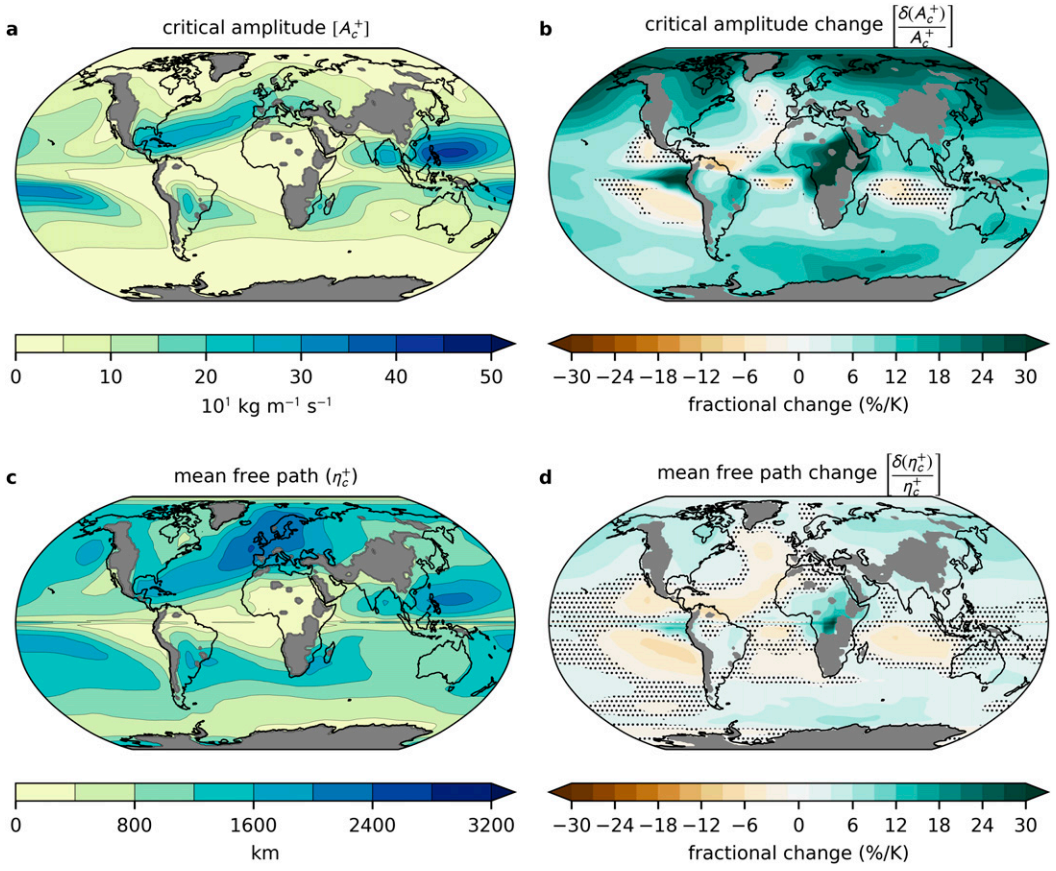

FIG. 9. Annual-mean, ensemble mean (a) present-day (1990–2005) reserved LHC, (b) RCP8.5 (2071–80) fractional change in the reserved LHC, (c) present-day mean free path, and (d) RCP8.5 fractional change in mean free path in CESM LENS. As in previous figures, land surface above 800 m is masked (gray shading) and stippling represents regions where fewer than 85% of the ensemble members agree on the sign.

intermodel spread. Future work will begin by evaluating models against these results and against reanalysis to identify dynamic sources of climatological bias. These dynamic contributors will then be compared to reanalysis data to further evaluate the simulated interactions between the large-scale circulation and the hydrologic cycle.

Acknowledgments. We would like to recognize comments by the editor and several anonymous reviewers that have improved the quality of this manuscript. We acknowledge the National Center for Atmospheric Research for its provision of CESM LENS data. Python libraries Numpy, matplotlib, xarray, and Cartopy were used extensively in the analysis and data visualization. Processing was performed on Indiana University supercomputers Karst, Carbonate, and Big Red II. S.S. and P.S. are supported under National Science Foundation Grant 1813981, and J.L. is supported by the U.S. Department of Energy Office of Science Biological and Environmental Research as part of the Regional and Global Modeling and Analysis Program.

Data availability statement. The 6-hourly CESM LENS data were downloaded from the National Center for Atmospheric Research and are publicly available upon request. Code for computing the wave activity budget is available from the corresponding author upon request.

REFERENCES

al Fahad, A., N. J. Burls, and Z. Strasberg, 2020: How will Southern Hemisphere subtropical anticyclones respond to global warming? Mechanisms and seasonality in CMIP5 and CMIP6 model projections. *Climate Dyn.*, **55**, 703–718, https://doi.org/10.1007/s00382-020-05290-7.

Algarra, I., J. Eiras-Barca, R. Nieto, and L. Gimeno, 2019: Global climatology of nocturnal low-level jets and associated moisture sources and sinks. *Atmos. Res.*, **229**, 39–59, https://doi.org/10.1016/j.atmosres.2019.06.016.

Allen, M. R., and W. J. Ingram, 2002: Constraints on future changes in climate and the hydrologic cycle. *Nature*, **419**, 228–232, https://doi.org/10.1038/nature01092.

Bony, S., G. Bellon, D. Klocke, S. Sherwood, S. Fermepin, and S. Denvil, 2013: Robust direct effect of carbon dioxide on tropical circulation and regional precipitation. *Nat. Geosci.*, **6**, 447–451, https://doi.org/10.1038/ngeo1799.

Bretherton, C. S., P. N. Blossey, and M. Khairoutdinov, 2005: An energy-balance analysis of deep convective self-aggregation

above uniform SST. *J. Atmos. Sci.*, **62**, 4273–4292, https://doi.org/10.1175/JAS3614.1.

Byrne, M. P., and P. A. O'Gorman, 2013: Land–ocean warming contrast over a wide range of climates: Convective quasi-equilibrium theory and idealized simulations. *J. Climate*, **26**, 4000–4016, https://doi.org/10.1175/JCLI-D-12-00262.1.

——, and ——, 2015: The response of precipitation minus evapotranspiration to climate warming: Why the ''wet-get-wetter, dry-get-drier'' scaling does not hold over land. *J. Climate*, **28**, 8078–8092, https://doi.org/10.1175/JCLI-D-15-0369.1.

Caballero, R., and J. Hanley, 2012: Midlatitude eddies, storm-track diffusivity, and poleward moisture transport in warm climates. *J. Atmos. Sci.*, **69**, 3237–3250, https://doi.org/10.1175/JAS-D-12-035.1.

Chang, E. K. M., Y. Guo, and X. Xia, 2012: CMIP5 multimodel ensemble projection of storm track change under global warming. *J. Geophys. Res.*, **117**, D23118, https://doi.org/10.1029/2012JD018578.

Chen, G., J. Norris, J. D. Neelin, J. Lu, L. R. Leung, and K. Sakaguchi, 2019: Thermodynamic and dynamic mechanisms for hydrological cycle intensification over the full probability distribution of precipitation events. *J. Atmos. Sci.*, **76**, 497–516, https://doi.org/10.1175/JAS-D-18-0067.1.

Feng, X., C. Liu, F. Xie, J. Lu, L. S. Chiu, G. Tintera, and B. Chen, 2019: Precipitation characteristic changes due to global warming in a high-resolution (16 km) ECMWF simulation. *Quart. J. Roy. Meteor. Soc.*, **145**, 303–317, https://doi.org/10.1002/qj.3432.

Gao, Y., J. Lu, L. R. Leung, Q. Yang, S. Hagos, and Y. Qian, 2015: Dynamical and thermodynamical modulations on future changes of landfalling atmospheric rivers over western North America. *Geophys. Res. Lett.*, **42**, 7179–7186, https://doi.org/10.1002/2015GL065435.

Hagos, S. M., L. R. Leung, J.-H. Yoon, J. Lu, and Y. Gao, 2016: A projection of changes in landfalling atmospheric river frequency and extreme precipitation over western North America from the large ensemble CESM simulations. *Geophys. Res. Lett.*, **43**, 1357–1363, https://doi.org/10.1002/2015GL067392.

He, C., B. Wu, L. Zou, and T. Zhou, 2017: Responses of the summertime subtropical anticyclones to global warming. *J. Climate*, **30**, 6465–6479, https://doi.org/10.1175/JCLI-D-16-0529.1.

He, J., and B. J. Soden, 2017: A re-examination of the projected subtropical precipitation decline. *Nat. Climate Change*, **7**, 53–57, https://doi.org/10.1038/nclimate3157.

Held, I. M., and B. J. Soden, 2000: Water vapor feedback and global warming. *Annu. Rev. Energy Environ.*, **25**, 441–475, https://doi.org/10.1146/annurev.energy.25.1.441.

——, and ——, 2006: Robust responses of the hydrological cycle to global warming. *J. Climate*, **19**, 5686–5699, https://doi.org/10.1175/JCLI3990.1.

Huang, C. S. Y., and N. Nakamura, 2016: Local finite-amplitude wave activity as a diagnostic of anomalous weather events. *J. Atmos. Sci.*, **73**, 211–229, https://doi.org/10.1175/JAS-D-15-0194.1.

——, and ——, 2017: Local wave activity budgets of the wintertime Northern Hemisphere: Implication for the Pacific and Atlantic storm tracks. *Geophys. Res. Lett.*, **44**, 5673–5682, https://doi.org/10.1002/2017GL073760.

Huang, P., D. Chen, and J. Ying, 2017: Weakening of the tropical atmospheric circulation response to local sea surface temperature anomalies under global warming. *J. Climate*, **30**, 8149–8158, https://doi.org/10.1175/JCLI-D-17-0171.1.

Joshi, M. M., J. M. Gregory, M. J. Webb, D. M. H. Sexton, and T. C. Johns, 2008: Mechanisms for the land/sea warming contrast exhibited by simulations of climate change. *Climate Dyn.*, **30**, 455–465, https://doi.org/10.1007/s00382-007-0306-1.

Kang, S. M., and J. Lu, 2012: Expansion of the Hadley cell under global warming: Winter versus summer. *J. Climate*, **25**, 8387–8393, https://doi.org/10.1175/JCLI-D-12-00323.1.

Kay, J. E., and Coauthors, 2014: The Community Earth System Model (CESM) large ensemble project: A community resource for studying climate change in the presence of internal climate variability. *Bull. Amer. Meteor. Soc.*, **96**, 1333–1349, https://doi.org/10.1175/BAMS-D-13-00255.1.

Kim, B.-M., and Coauthors, 2014: Weakening of the stratospheric polar vortex by Arctic sea-ice loss. *Nat. Commun.*, **5**, 4646, https://doi.org/10.1038/ncomms5646.

Liu, B., X. Tan, T. Y. Gan, X. Chen, K. Lin, M. Lu, and Z. Liu, 2020: Global atmospheric moisture transport associated with precipitation extremes: Mechanisms and climate change impacts. *Wiley Interdiscip. Rev.: Water*, **7**, e1412, https://doi.org/10.1002/wat2.1412.

Lorenz, D. J., and E. T. DeWeaver, 2007: The response of the extratropical hydrological cycle to global warming. *J. Climate*, **20**, 3470–3484, https://doi.org/10.1175/JCLI4192.1.

Lu, J., G. A. Vecchi, and T. Reichler, 2007: Expansion of the Hadley cell under global warming. *Geophys. Res. Lett.*, **34**, L06805, https://doi.org/10.1029/2006GL028443.

——, and Coauthors, 2014: The robust dynamical contribution to precipitation extremes in idealized warming simulations across model resolutions. *Geophys. Res. Lett.*, **41**, 2971–2978, https://doi.org/10.1002/2014GL059532.

——, and Coauthors, 2017: Examining the hydrological variations in an aquaplanet world using wave activity transformation. *J. Climate*, **30**, 2559–2576, https://doi.org/10.1175/JCLI-D-16-0561.1.

——, D. Xue, Y. Gao, G. Chen, L. R. Leung, and P. Staten, 2018: Enhanced hydrological extremes in the western United States under global warming through the lens of water vapor wave activity. *npj Climate Atmos. Sci.*, **1**, 7, https://doi.org/10.1038/s41612-018-0017-9.

Menary, M. B., and R. A. Wood, 2018: An anatomy of the projected North Atlantic warming hole in CMIP5 models. *Climate Dyn.*, **50**, 3063–3080, https://doi.org/10.1007/s00382-017-3793-8.

Nakamura, N., and A. Solomon, 2010: Finite-amplitude wave activity and mean flow adjustments in the atmospheric general circulation. Part I: Quasigeostrophic theory and analysis. *J. Atmos. Sci.*, **67**, 3967–3983, https://doi.org/10.1175/2010JAS3503.1.

Neelin, J. D., and Coauthors, 2010: Long tails in deep columns of natural and anthropogenic tropospheric tracers. *Geophys. Res. Lett.*, **37**, L05804, https://doi.org/10.1029/2009GL041726.

——, B. Langenbrunner, J. E. Meyerson, A. Hall, and N. Berg, 2013: California winter precipitation change under global warming in the Coupled Model Intercomparison Project phase 5 ensemble. *J. Climate*, **26**, 6238–6256, https://doi.org/10.1175/JCLI-D-12-00514.1.

O'Gorman, P. A., 2015: Precipitation extremes under climate change. *Curr. Climate Change Rep.*, **1**, 49–59, https://doi.org/10.1007/s40641-015-0009-3.

——, and T. Schneider, 2009: The physical basis for increases in precipitation extremes in simulations of 21st-century climate change. *Proc. Natl. Acad. Sci. USA*, **106**, 14 773–14 777, https://doi.org/10.1073/pnas.0907610106.

——, and C. J. Muller, 2010: How closely do changes in surface and column water vapor follow Clausius–Clapeyron scaling in climate change simulations? *Environ. Res. Lett.*, **5**, 025207, https://doi.org/10.1088/1748-9326/5/2/025207.

Peings, Y., J. Cattiaux, S. Vavrus, and G. Magnusdottir, 2017: Late twenty-first-century changes in the midlatitude atmospheric circulation in the CESM large ensemble. *J. Climate*, **30**, 5943–5960, https://doi.org/10.1175/JCLI-D-16-0340.1.

Pendergrass, A. G., and E. P. Gerber, 2016: The rain is askew: Two idealized models relating vertical velocity and precipitation distributions in a warming world. *J. Climate*, **29**, 6445–6462, https://doi.org/10.1175/JCLI-D-16-0097.1.

Pfahl, S., P. A. O'Gorman, and E. M. Fischer, 2017: Understanding the regional pattern of projected future changes in extreme precipitation. *Nat. Climate Change*, **7**, 423–427, https://doi.org/10.1038/nclimate3287.

Polade, S. D., D. W. Pierce, D. R. Cayan, A. Gershunov, and M. D. Dettinger, 2014: The key role of dry days in changing regional climate and precipitation regimes. *Sci. Rep.*, **4**, 4364, https://doi.org/10.1038/srep04364.

——, A. Gershunov, D. R. Cayan, M. D. Dettinger, and D. W. Pierce, 2017: Precipitation in a warming world: Assessing projected hydro-climate changes in California and other Mediterranean climate regions. *Sci. Rep.*, **7**, 10783, https://doi.org/10.1038/s41598-017-11285-y.

Romanowsky, E., and Coauthors, 2019: The role of stratospheric ozone for Arctic–midlatitude linkages. *Sci. Rep.*, **9**, 7962, https://doi.org/10.1038/s41598-019-43823-1.

Scheff, J., and D. M. W. Frierson, 2012: Robust future precipitation declines in CMIP5 largely reflect the poleward expansion of model subtropical dry zones. *Geophys. Res. Lett.*, **39**, L18704, https://doi.org/10.1029/2012GL052910.

——, and ——, 2014: Scaling potential evapotranspiration with greenhouse warming. *J. Climate*, **27**, 1539–1558, https://doi.org/10.1175/JCLI-D-13-00233.1.

Seager, R., and N. Henderson, 2013: Diagnostic computation of moisture budgets in the ERA-Interim reanalysis with reference to analysis of CMIP-archived atmospheric model data. *J. Climate*, **26**, 7876–7901, https://doi.org/10.1175/JCLI-D-13-00018.1.

——, N. Naik, and G. A. Vecchi, 2010: Thermodynamic and dynamic mechanisms for large-scale changes in the hydrological cycle in response to global warming. *J. Climate*, **23**, 4651–4668, https://doi.org/10.1175/2010JCLI3655.1.

Shaw, T. A., 2019: Mechanisms of future predicted changes in the zonal mean mid-latitude circulation. *Curr. Climate Change Rep.*, **5**, 345–357, https://doi.org/10.1007/s40641-019-00145-8.

——, and Coauthors, 2016: Storm track processes and the opposing influences of climate change. *Nat. Geosci.*, **9**, 656–664, https://doi.org/10.1038/ngeo2783.

Shepherd, T. G., 2014: Atmospheric circulation as a source of uncertainty in climate change projections. *Nat. Geosci.*, **7**, 703–708, https://doi.org/10.1038/ngeo2253.

Singh, M. S., and P. A. O'Gorman, 2012: Upward shift of the atmospheric general circulation under global warming: Theory and simulations. *J. Climate*, **25**, 8259–8276, https://doi.org/10.1175/JCLI-D-11-00699.1.

Song, F., L. R. Leung, J. Lu, and L. Dong, 2018: Seasonally dependent responses of subtropical highs and tropical rainfall to anthropogenic warming. *Nat. Climate Change*, **8**, 787–792, https://doi.org/10.1038/s41558-018-0244-4.

Staten, P. W., K. M. Grise, S. M. Davis, K. Karnauskas, and N. Davis, 2019: Regional widening of tropical overturning: Forced change, natural variability, and recent trends. *J. Geophys. Res. Atmos.*, **124**, 6104–6119, https://doi.org/10.1029/2018JD030100.

Stephens, G. L., and Y. Hu, 2010: Are climate-related changes to the character of global-mean precipitation predictable? *Environ. Res. Lett.*, **5**, 025209, https://doi.org/10.1088/1748-9326/5/2/025209.

Swanson, K. L., and R. T. Pierrehumbert, 1997: Lower-tropospheric heat transport in the Pacific storm track. *J. Atmos. Sci.*, **54**, 1533–1543, https://doi.org/10.1175/1520-0469(1997)054<1533:LTHTIT>2.0.CO;2.

Tamarin-Brodsky, T., and Y. Kaspi, 2017: Enhanced poleward propagation of storms under climate change. *Nat. Geosci.*, **10**, 908–913, https://doi.org/10.1038/s41561-017-0001-8.

——, and O. Hadas, 2019: The asymmetry of vertical velocity in current and future climate. *Geophys. Res. Lett.*, **46**, 374–382, https://doi.org/10.1029/2018GL080363.

Tandon, N. F., X. Zhang, and A. H. Sobel, 2018: Understanding the dynamics of future changes in extreme precipitation intensity. *Geophys. Res. Lett.*, **45**, 2870–2878, https://doi.org/10.1002/2017GL076361.

Thackeray, C. W., A. M. DeAngelis, A. Hall, D. L. Swain, and X. Qu, 2018: On the connection between global hydrologic sensitivity and regional wet extremes. *Geophys. Res. Lett.*, **45**, 11 343–11 351, https://doi.org/10.1029/2018GL079698.

Trenberth, K. E., 1999: Conceptual framework for changes of extremes of the hydrological cycle with climate change. *Climatic Change*, **42**, 327–339, https://doi.org/10.1023/A:1005488920935.

——, and C. J. Guillemot, 1995: Evaluation of the global atmospheric moisture budget as seen from analyses. *J. Climate*, **8**, 2255–2272, https://doi.org/10.1175/1520-0442(1995)008<2255:EOTGAM>2.0.CO;2.

Vallis, G. K., 2006: *Atmospheric and Oceanic Fluid Dynamics*. 1st ed. Cambridge University Press, 770 pp.

Vecchi, G. A., and B. J. Soden, 2007: Global warming and the weakening of the tropical circulation. *J. Climate*, **20**, 4316–4340, https://doi.org/10.1175/JCLI4258.1.

Wang, J., H.-M. Kim, and E. K. M. Chang, 2017: Changes in Northern Hemisphere winter storm tracks under the background of Arctic amplification. *J. Climate*, **30**, 3705–3724, https://doi.org/10.1175/JCLI-D-16-0650.1.

Weller, E., C. Jakob, and M. J. Reeder, 2019: Understanding the dynamic contribution to future changes in tropical precipitation from low-level convergence lines. *Geophys. Res. Lett.*, **46**, 2196–2203, https://doi.org/10.1029/2018GL080813.

Wills, R. C., M. P. Byrne, and T. Schneider, 2016: Thermodynamic and dynamic controls on changes in the zonally anomalous hydrological cycle. *Geophys. Res. Lett.*, **43**, 4640–4649, https://doi.org/10.1002/2016GL068418.

Xue, D., J. Lu, L. R. Leung, and Y. Zhang, 2018: Response of the hydrological cycle in Asian monsoon systems to global warming through the lens of water vapor wave activity analysis. *Geophys. Res. Lett.*, **45**, 11 904–11 912, https://doi.org/10.1029/2018GL078998.

Yettella, V., and J. E. Kay, 2017: How will precipitation change in extratropical cyclones as the planet warms? Insights from a large initial condition climate model ensemble. *Climate Dyn.*, **49**, 1765–1781, https://doi.org/10.1007/s00382-016-3410-2.

Zhu, Y., and R. E. Newell, 1998: A proposed algorithm for moisture fluxes from atmospheric rivers. *Mon. Wea. Rev.*, **126**, 725–735, https://doi.org/10.1175/1520-0493(1998)126<0725:APAFMF>2.0.CO;2.